Three-dimensional reconstruction of wear debris by multi-view contour fitting and dense point-cloud interpolation

Yeping Peng[a,*], Zhengbin Wu[a], Guangzhong Cao[a,*], Song Wang[b,*], Hongkun Wu[c], Chaozong Liu[d], Zhongxiao Peng[c]

[a] *Guangdong Key Laboratory of Electromagnetic Control and Intelligent Robots, College of Mechatronics and Control Engineering, Shenzhen University, Shenzhen 518060, China*

[b] *Biomechanics and Biotechnology Lab, Research Institute of Tsinghua University in Shenzhen, Shenzhen 518057, China*

[c] *School of Mechanical and Manufacturing Engineering, The University of New South Wales, Sydney, NSW 2052, Australia*

[d] *Institute of Orthopaedics and Musculoskeletal Science, University College London, London, WC1E 6BT, UK*

Abstract: Three-dimensional (3D) surfaces of wear particles were reconstructed through multi-view contour fitting and dense point-cloud interpolation with an aim to obtain comprehensive features for wear debris analysis. Multiple image frames at different views were captured when the particles move with rotations through a micro-sized flow channel. The particle contours were extracted from multi-view images to build a 3D model based on particle contour fitting. The 3D modeling accuracy was then improved through an interpolated dense point-cloud. To validate the 3D model, an experiment was carried out to compare the performance of the 3D model to that of results obtained using laser scanning confocal microscopy. The results show that the errors of quantitative surface characterization using the arithmetical mean height (Sa) and the root-mean-square height (Sq) are less than 5.86%, and less than 17.12% for the kurtosis (Sku). The proposed 3D wear debris analysis has great potential in online condition monitoring of wear particles.

***Keywords*:** Wear particle analysis, 3D reconstruction, Multi-view contour fitting, Dense point-cloud interpolation

[*]Corresponding author, Email addresses: pyp8020@163.com (Yeping Peng), gzcao@szu.edu.cn (Guangzhong Cao), wangs@tsinghua-sz.org (Song Wang)

1. Introduction

Wear debris analysis (WDA) is an important technique for wear analysis in both off-line and on-line condition monitoring [1-3]. The wear particle features, including size, shape, color and surface texture, are critical indicators of wear severity and wear mechanism [4-6]. Correspondingly, ferrography has been developed and used for WDA to acquire morphology features of wear particles [7]. However, most of existing ferrograph image analysis methods are based on two-dimensional (2D) characterization, making it difficult or impossible to quantitatively measure their surface features in which 3D surface data is required.

With the development of 3D scanning techniques, 3D characterization of wear particles was realized by utilizing laser scanning confocal microscopy (LSCM) [8] and atomic force microscopy (AFM) [9]. However, these instruments are expensive and their complex operations are time-consuming, making them difficult to be popularized in industrial applications. In order to reduce the dependence on scanning techniques, 3D image reconstruction algorithms were employed to construct the 3D surface shape of wear debris based on photometric stereo [10]. Whereas, images obtained in a single direction cannot provide some important 3D information, such as thickness and volume, leading to the incorrect characterization of wear particles.

To overcome problems encountered in 3D particle characterization, multi-view images of moving particles in rolling motions were captured to estimate the particle thickness and volume [11]. To improve the 3D modeling accuracy, image restoration [12-14] was performed to improve image quality. Meanwhile, the particle movements were simulated to obtain the motion parameters for 3D reconstruction. However, these methods cannot be directly applied to online WDA because they are dependent on feature extraction from high-resolution images captured using a microscope.

In our previous work, a microfluidic device was designed to image moving wear debris for online 3D analysis [15]. Based on this, 3D characteristics of wear particles (e.g., thickness, height aspect ratio, special dimension and sphericity) were constructed for online WDA and wear particle identification [16-18]. However, the uncertainties of particle rolling motion and low-resolution images may introduce significant errors in 3D wear debris analysis (3D-WDA) in online condition monitoring.

In order to address the issues associate with 3D-WDA, this work is focused on developing a method for 3D particle reconstruction by combining multi-view contour fitting and point-cloud interpolation. Firstly, two basic parameters, including the rotation axis and rotation angle, were used to reconstruct the 3D particle model based on multi-view contour fitting. For this purpose, particle motions were analyzed to determine the rotation axis of moving wear particles. Meanwhile, the similarity of the multi-view contours is analyzed to estimate the rotation angles between two consecutive image frames. Secondly, the sparse 3D point-cloud model of wear particle was constructed by multi-view contour fitting based on the rotation axis and the rotation angle. Finally, the 3D reconstruction accuracy was improved using dense point-cloud interpolation.

The rest of the paper is organized as follows. Section 2 describes the moving particle imaging system and multi-view image acquisition process. Section 3 presents the proposed method of wear particle reconstruction in three dimensions. The experiment is described and results are discussed in Section 4. The conclusion is given in Section 5.

2. Multi-view image acquisition of moving wear particles

Image reconstruction using a sequence of images at different views is a useful technology for 3D image analysis [19]. For 3D characterization of wear debris, a moving particle imaging system [20] was

designed to capture multi-view particle images, as shown in Fig. 1. Six main parts of the imaging system are an oil flow path, a digital pump, oil pipes, an oil tank containing oil with wear particles, a CMOS imaging sensor and a computer.

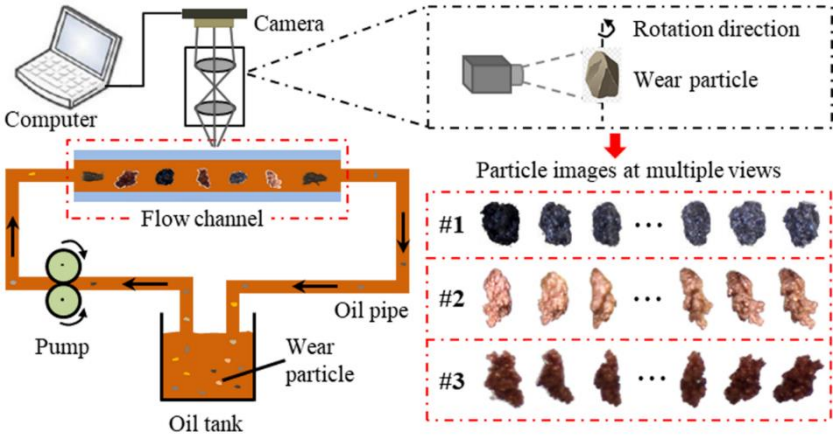

Figure 1: Schematic diagram of moving particle imaging system.

The lubrication oil in an oil tank is driven by the digital pump to the oil flow channel, which contributes the oil circuit system. Wear particles carried in the lubrication oil are captured by the CMOS camera when they pass through the flow channel. The flow channel is designed to ensure that the fluid flow is laminar, and the particles are in rolling movements. Hence, the particle images can be captured from different directions for multi-view image acquisition.

The wear particles are collected from wear tests with metallic pin-on-disc pairs under different working conditions including lubrication, loading, and running speed. The particles in the range of 20 to 200 μm are detected and imaged. The video frame rate is 30 frame per second (fps). The image resolution is 1920 × 1080 pixels, and the particle resolution reaches 0.396 μm. The quantity of oil flow is less than 1 mL/min to avoid image motion blur. Meanwhile, the particle concentration, which is indexed using particle area occupation to the image, is controlled in the range of 0.02 to 0.05 μm based on experimental result. This is to guarantee target particle acquisition and avoid particle collision in the flow channel.

More details of the moving particle imaging system and the oil channel structure can be found in references [15, 21].

The image sequences of three particles (Fig. 1) have different surface and contour morphologies. It was observed from Fig. 1 that feature extraction from different view images is important to improve the analysis accuracy of irregular particles. For wear debris analysis at different views, a method of 3D reconstruction using image sequence is proposed and described in the next section.

3. 3D wear particle reconstruction

The 3D model of wear particle is reconstructed using image sequences at different views. Fig. 2 shows the flowchart of the proposed method. Multiple images captured at different views are used as input. First, motion parameters of the moving particle including the rotation axis and angle, are determined based on motion analysis and feature matching. Second, the particle contours are extracted from different view images and are used to construct the 3D model of wear particle by contour fitting. Finally, a dense point-cloud is generated using interpolation to improve the 3D reconstruction accuracy.

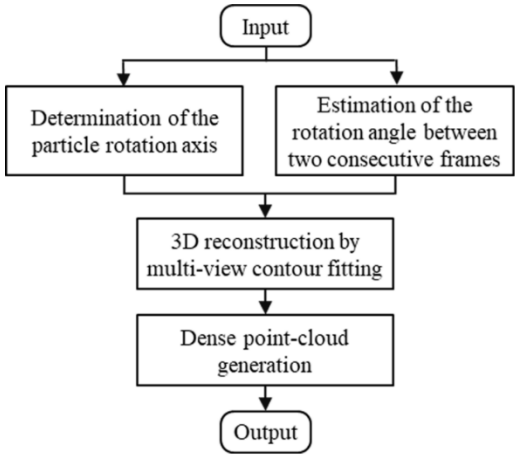

Figure 2: Flowchart of the proposed 3D particle reconstruction method.

3.1. Determination of the rotation axis

The rotation axis is the basis of multi-view contour fitting for 3D reconstruction of wear particles. In order to determine this axis, the motion characteristics of moving wear particles are analyzed.

Fig. 3 shows the motion scenario of the lubrication oil and particles. The oil flow is laminar when the fluid Reynolds number is less than 2300 [22]. In general, the metallic particles flow along the channel bottom due to the metallic density is much higher than its carrying medium oil. Consider two particles with centroid P_1 and P_2, particle #1 is suspending from the channel bottom, and particle #2 is along the channel bottom.

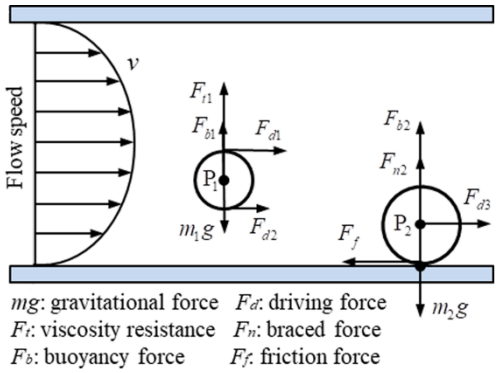

Figure 3: Flow scenario of particles inside the flow channel.

The driving force (F_d) caused by the flowing fluid is defined as [23]

$$F_d = \frac{C_d v^2 \rho_l A}{2} \tag{1}$$

where C_d is scouring coefficient, A is the projected area of the particle normal to flow direction.

To simplify the force analysis, the particle cross-sections are assumed as circular, and the radius is R_d. Then the rolling moments of the two particles can be expressed as:

$$M_1 = (F_{d1} - F_{d2})R_1 \tag{2}$$

$$M_2 = F_{d3}R_2 \tag{3}$$

According to the distribution of flow speed shown in Fig. 3, we have $F_{d1} > F_{d2}$. The particles are

both acted on by the rolling moments, making the particles to move with rotation. Under the rotation scenario, the particles are imaged using the CMOS camera shown in Fig. 1, and multiple images at different views are obtained. Fig. 4 shows multi-view images and the extracted contours of an ellipse-like particle. The contour sequence shows that the multiple images can be regarded as rotating about a basic axis, which is marked with a red dot-dash line. The basic axis is normal to the particle moving direction and passes through the centroid of the cross-section.

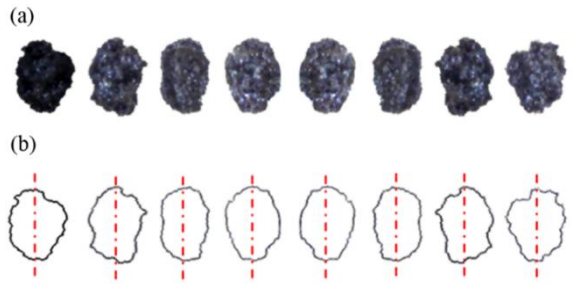

Figure 4: Multi-view images and the extracted contours of an ellipse-like particle: (a) multi-view images; (b) image contours at different views.

Based on the basic axis, a three-axis coordinate system can be built using the contour sequence and multi-view contour fitting. The 3D construction process is shown in Fig. 5. It can be seen that the basic axis is used as the rotation axis of the 3D model. Besides, the rotation angle between two adjacent images is also the basic parameter of the 3D reconstruction, which needs to be acquired.

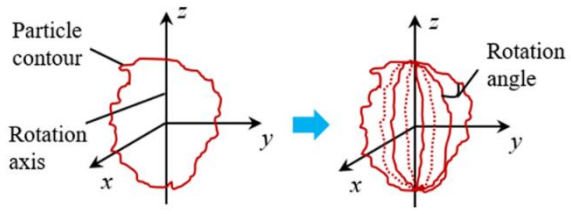

Figure 5: Illustration of 3D reconstruction by multi-view contour fitting.

It worth to mention that the particles' movement is random because the local turbulent flow of the fluid is produced when the particle moves. The complex fluid flow also changes the particle motion

direction. In the reconstruction process, the basic axis of different image contours is adjusted and combined by utilizing the matching of contour features.

3.2. Estimation of the rotation angle between adjacent images

To estimate the particle rotation angle, the first captured image is referred to the base image and its angle is regarded as 0°. Then the images with 90° and 180° can be examined according to the similarity of particle contours. The 180° image has a mirror symmetric contour to the 0° image, and the 90° image has the highest deviation from the 0° and 180° images.

The second-order image moments are widely used to express the central moment of target objects, which are suitable to describe the similarity of particle contours. In particular, Hu moments calculated by image moments are invariant in translation, rotation and scale. Therefore, the Hu moment (H) obtained by the second-order image moments is used as the indicator of image similarity, which is [24]

$$H = (\eta_{20} - \eta_{02})^2 + 4\eta_{11}^2 \tag{4}$$

where, η_{pq} is the normalized $(p + q)$-order image moment, and $p + q = 2$. Therein,

$$\eta_{pq} = \frac{m_{pq}}{m_{00}^2} \tag{5}$$

where, m_{pq} is the $(p + q)$-order image moment, which is calculated by

$$m_{pq} = \sum\sum (x - \overline{x})^p (y - \overline{y})^q M(x, y) \tag{6}$$

where, (x, y) is the coordinate of image pixels; $M(x, y)$ is a binarized image; $(\overline{x}, \overline{y})$ is the centroid coordinate.

In practice, translation and rotation generally occur at the same time when the particles move within the lubrication oil. The particle images captured in translation motions have similar shapes, which will affect the accuracy of rotation angle estimation. Hence, the adjacent images with similar particle contours

need to be identified and discarded. For example, there are 80 images of the particle shown in Fig. 4. The deviations of H values between two adjacent images are calculated and their normalized results (H_1) are shown in Fig. 6. It can be seen that some H_1 values are close to zero, which indicates that the adjacent images have similar contours.

A threshold should be determined to judge whether the images have the same contour shape. In this work, the threshold is defined as the value when the sum of the difference between the threshold and the H_1 values is the minimum. For the H_1 shown in Fig. 6, the threshold is interactively calculated and set to 0.23. Based on this, the translation images ($H_1 < 0.23$) are deleted, and the rotation images ($H_1 \geq 0.23$) are obtained.

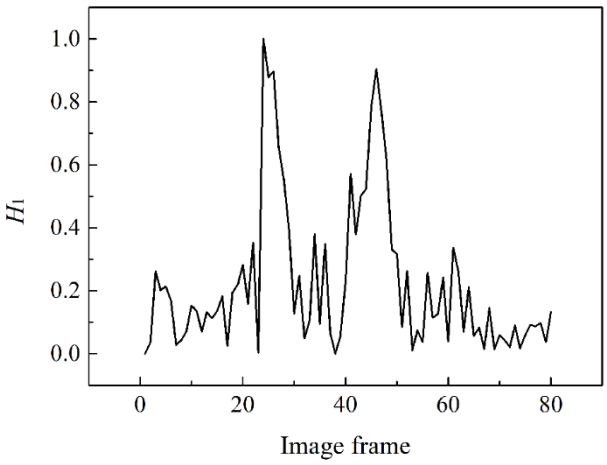

Figure 6: The H_1 values between two adjacent images of the particle shown in Fig. 4.

In order to find out the 90° and 180° images, the absolute deviation of H values between the rotation images to the reference image (the first frame) are calculated and normalized, as shown in Fig. 7. It can be seen that the particle rotates more than half a turn. The 11-th image frame and the 23-th image frame have the highest and the lowest deviations to the first frame, respectively. Hence, the 11-th and the 23-th images are the 90° and the 180° images respectively.

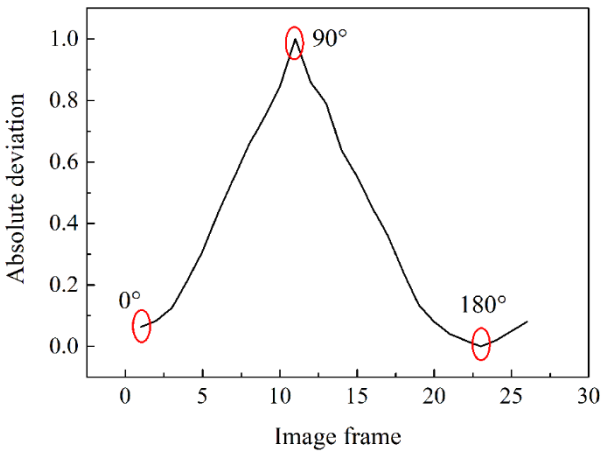

Figure 7: Absolute deviations of *H* values of acquired images to the reference image.

It can be seen from Fig. 7, there are local oscillations on the deviation. This is due to the image moments are affected by particle image segmentation. The image segmentation accuracy will influence the accuracy of rotation image identification. On the other hand, random rolling movements and irregular shapes of wear particles increase the complexity of rotation analysis. In order to estimate the rotation angle between two adjacent images, the particle motions are simplified and regarded as uniform rolling movements. In this case, the rotation angles are assumed equally distributed between the number of frames between the 0° and 180° images. The angles of all the rotation images to the reference image are

$$\theta_i = \frac{180}{n-1}(i-1), i = 1, 2, \ldots, n \tag{7}$$

where θ_i is the angle of the *i*-th image to the reference image, *n* is the number of images between the 0° image and 180° image.

It is noted that more than 360 rotate degrees may be produced during the particle rotation movements. Considering that the particle rotation axis is influenced by the particle shape and the oil flow conditions, the particle contours extracted from the 180°~360° images may be different to those of 0°~180° images. In order to reduce the error caused by contour fitting, only the 0°~180° image sequence is extracted and used to construct the particle model.

3.3. Three-dimensional reconstruction by multi-view contour fitting

Based on the results of rotation axis determination and rotation angle estimation, the particle can be reconstructed in 3D using its multiple image contours. The process of multi-view contour fitting is illustrated in Fig. 5. Assume that the coordinate of a pixel P located at the i-th image contour is $P({u_p}^i, {v_p}^i)$, the centroid coordinate of the i-th image is $C(\bar{u}_i, \bar{v}_i)$. Then the special coordinates of the pixel P can be acquired from

$$\begin{cases} {x_p}^i = \lambda({u_p}^i - \bar{u}_i)\sin\theta_i \\ {y_p}^i = \lambda({u_p}^i - \bar{u}_i)\cos\theta_i \\ {z_p}^i = \lambda({v_p}^i - \bar{v}_i) \end{cases}$$

where λ is a pixel scale factor that can be obtained by camera calibration.

All the pixels of the contour sequence extracted from a series of rotation images are translated to the spatial coordinate system. Then a 3D particle model is established, as shown in Fig. 8. It was observed that the particle model has high accuracy on the contour shape. However, it can be seen openings on the model surface. This is because the 3D model is built only using the image contour points while the surface information is not available. Therefore, the rotation angle between two adjacent images is an important factor affecting the 3D reconstruction accuracy. Correspondingly, the quantity of oil flow is controlled according to the frame rate of CMOS camera to ensure that the image frame number during the imaging process. In this study, the frame number of 0°-to-180° images should be larger than 15 to narrow the gap of particle contours. For further repairing the surface openings to improve the reconstruction accuracy, a dense point-cloud from the 3D model is generated, which will be described in the next section.

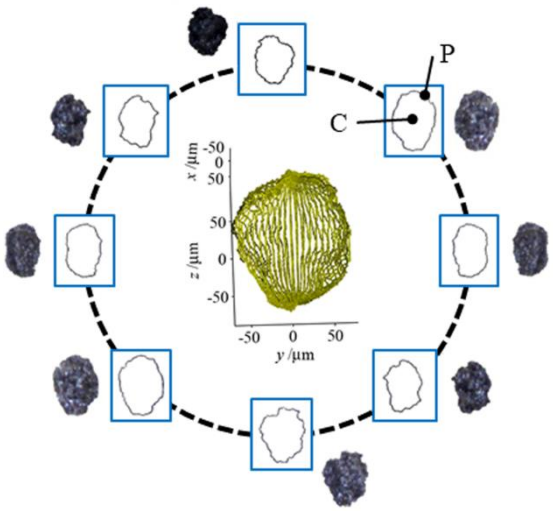

Figure 8: Demonstration of 3D reconstruction of the wear particle shown in Fig. 4.

3.4. Dense point-cloud generation from the constructed 3D particle model

Interpolation approaches [25-27] are commonly used to generate dense points in 3D image reconstruction. For the 3D model constructed by image contours, it can be divided into a series of sparse point layers whose number is equal to half the number of the pixels in one image contour. The number of points in each layer is twice the number of image frames, as demonstrated in Fig. 9. Correspondingly, an interpolation method based on curve fitting is developed to generate more points for 3D dense reconstruction.

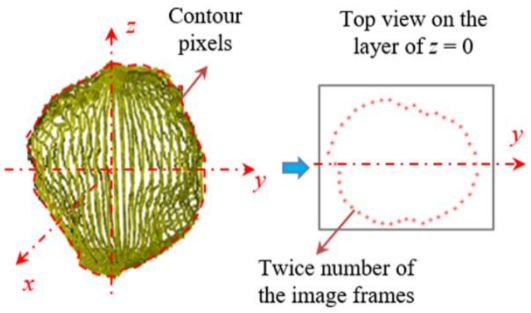

Figure 9: Construction of the 3D model using image contours.

The regression spline [28] is employed as the curve fitting method because of its flexibility and the production of smooth curves. In particular, the natural cubic spline (NCS) is one of the most widely used

spline functions [29]. After processed by the NCS method, the curve fitting result of the $z = 0$ layer is obtained and shown in Fig. 10(b). As shown in Fig. 10, a smooth fitting curve is obtained.

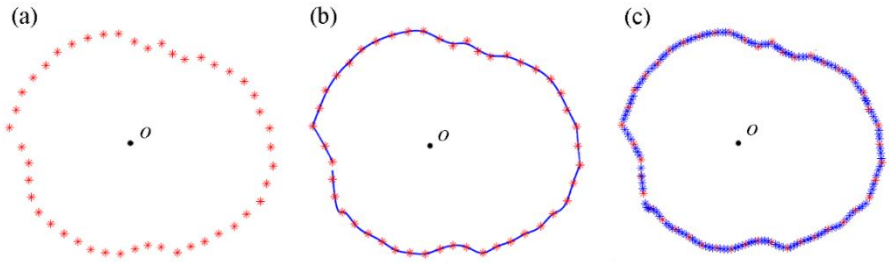

Figure 10: Dense point-cloud generated by the NCS-based interpolation on the $z = 0$ layer: (a) original points; (b) NCS curve fitting; (c) interpolated points.

Afterwards, interpolation is conducted to generate more points. As mentioned above, the 3D point-cloud is produced by image contour pixels. Hence, the number of interpolated points is determined according to the contour pixel characteristics, i.e. the distance between two adjacent points after interpolation should be reduced. Based on this, the dense points of the $z = 0$ layer are generated, and the results are shown in Fig. 10(c). The points marked in blue are the interpolated points. The number of points (176) after interpolation is increased by about four times (46 points).

The NCS-based interpolation is applied to all the 3D model layers, and a dense point-cloud model is obtained, as shown in Fig. 11(b). There are 6523 points on the sparse point-cloud model. After the dense point-cloud generation, the openings on the sparse point-cloud model have been repaired, and the number of points reaches 14965, which is more than twice of the original. Meanwhile, the particle contour shape is maintained, which is helpful to improve the 3D reconstruction accuracy.

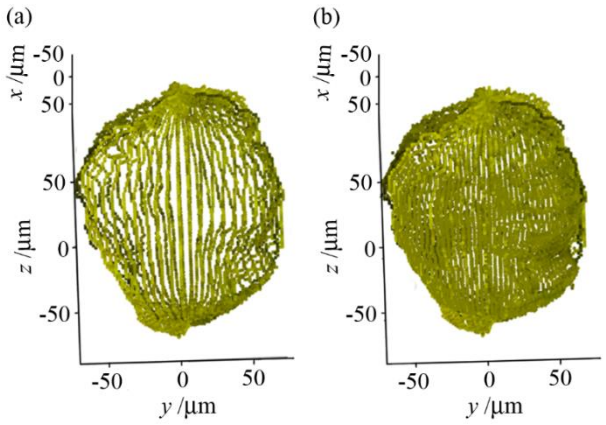

Figure 11: Comparison of the sparse and dense point-cloud: (a) sparse point-cloud; (b) dense point-cloud.

4. Experiment and discussion

A LSCM was used to extract the 3D morphologies of wear particles in a high resolution to compare the performance of the proposed method. The 3D particle images were captured using the LSCM when the lubrication oil was not flowing (the oil pump was powered off). After the 3D imaging of static particles, the pump was powered on and the particles began to move. At the same time, the moving particles were captured and saved as videos. Then the rotating particles were identified, their multi-view images were used to construct the 3D point-cloud using the proposed method. Finally, a comparative experiment was carried out on the LSCM results and the reconstructed results to evaluate the effectiveness of the proposed 3D reconstruction method.

The LSCM images and reconstructed 3D models of particle samples are shown in Fig. 12. Multiple images of each particle were captured at different views, as shown in Fig. 12(a). However, only the single-view LSCM image of each particle was acquired, which can be seen in Fig. 12(b). This is because the LSCM image were captured when the particles were stationary. This indicates that only the first image frame can be used to compare the LSCM and the reconstruction results. Hence, the sparse and the dense point-cloud models were shown at the same view as the LSCM image, as shown in Fig. 12(c) and

Fig. 12(d). It can be seen that the reconstructed 3D models have similar shapes to the LSCM images.

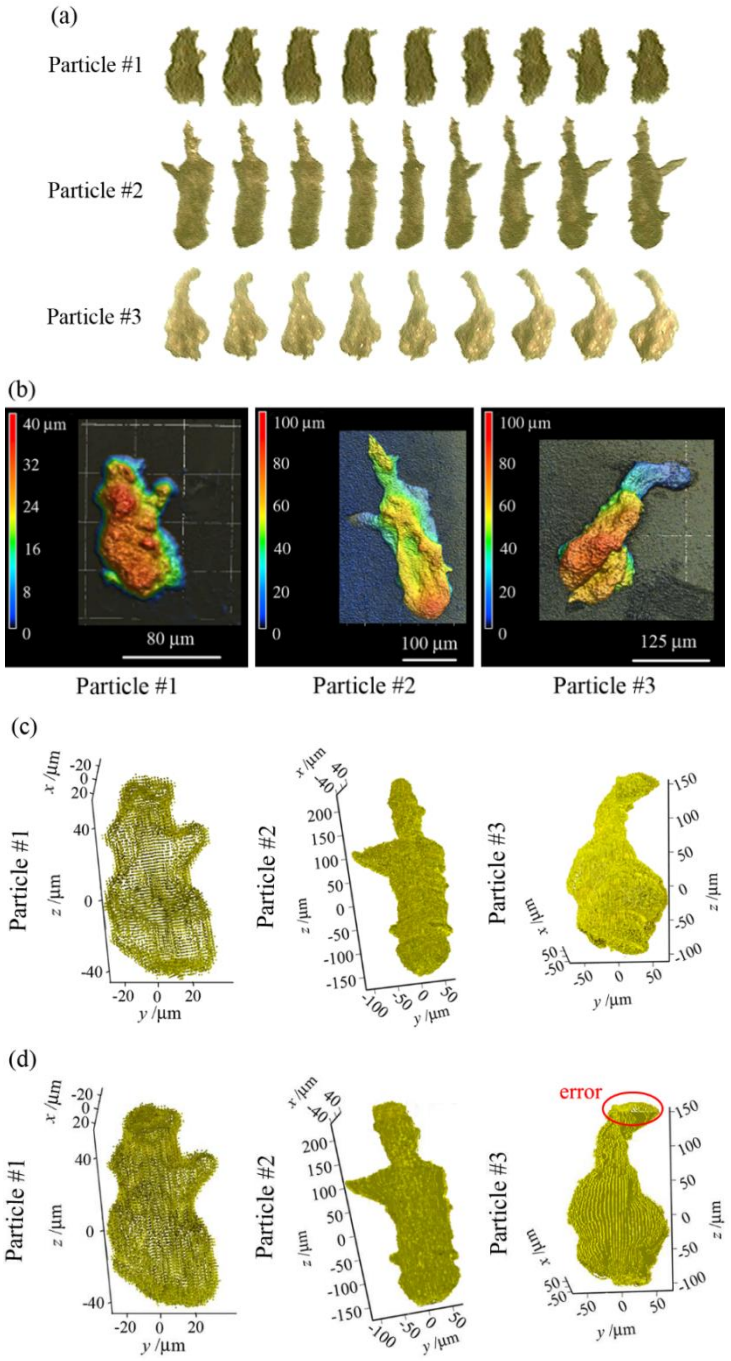

Figure 12: Three example particles: LSCM images and reconstructed 3D models: (a) multi-view images captured using the system shown in Fig. 1; (b) LSCM images; (c) Sparse point-cloud models; (d) Dense point-cloud models.

It was observed from Fig. 12(c) and Fig. 12(d), the constructed point-cloud models of particle # 2 and particle # 3 are denser than that of particle # 1. This is because the size of particle # 1 (long-axis of

105 μm) is much smaller than that of particle # 2 (long-axis about 406 μm) and particle # 3 (long-axis about 259 μm), therefore the number of points is much less than particle # 2 and particle # 3.

To quantitatively analyze the experimental results, the particle surface morphologies obtained by the LSCM and the proposed reconstruction method are both characterized using the indicators including arithmetical mean height (Sa), the root-mean-square height (Sq) and the kurtosis (Sku) [30]. The results are listed in Table 1. The 'Error-Sparse' and 'Error-Dense' respectively denote the errors of the sparse and the dense point-cloud models compared to the LSCM models.

Table 1: Particle surface morphologies of the LSCM and the reconstructed models.

Particle	Indicator	LSCM	Sparse	Dense	Error-Sparse (%)**	Error-Dense (%)**
Particle #1	Sa (μm)	8.12	7.87	8.08	3.08	0.49
	Sq (μm)	9.62	9.31	9.79	3.22	1.77
	Sku (μm^{-2})	2.54	2.11	2.18	16.93	14.17
Particle #2	Sa (μm)	14.83	14.52	14.61	2.09	1.48
	Sq (μm)	19.13	18.04	18.20	5.70	4.86
	Sku (μm^{-2})	2.95	2.57	2.58	12.88	12.54
Particle #3	Sa (μm)	19.96	21.58	19.73	8.12	1.15
	Sq (μm)	25.59	25.66	24.09	0.27	5.86
	Sku (μm^{-2})	2.92	2.28	2.42	21.92	17.12

** $Error - Sparse = \frac{|Sparse - LSCM|}{LSCM}$, and $Error - Dense = \frac{|Dense - LSCM|}{LSCM}$

It can be seen that the Sku has higher errors (larger than 12.54%), in both the sparse models and dense models than the Sa and Sq errors (less than 5.86%). From Fig. 12(a) and Fig. 12(b), it can be seen that the LSCM model surfaces are acquired from the first frame image under static conditions, and the LSCM models are the local regions of the particle surfaces. The information extracted from only one single-view image cannot completely characterize the particle morphologies in 3D. Compared to the LSCM models, the 3D models reconstructed using multi-view images may have larger contours and lead to high deviations on the kurtosis to the LSCM models.

It can also be seen that most of the errors of sparse models are in the range of 0.27% to 21.92%, which are significantly reduced to the range of 0.49% to 17.12% after using the dense point-cloud. Whereas, the Sq of particle # 3 is increased from 0.27% (error-sparse) to 5.86% (error-dense). This is caused by the error of dense point-cloud at the top of particle # 3, which is shown in Fig. 12(d). The dense point-cloud on the spindly regions needs to be optimized in the future. In short, the proposed method can provide high accuracy 3D models of wear particles, and the Sa and Sq errors of dense models are less than 5.86%. Furthermore, the 3D particle models obtained by the proposed method can provide more information than conventional 3D models at a single-view, which has great values in improving the accuracy of wear particle analysis and wear mechanism assessment.

5. Conclusion

The 3D image reconstruction method for wear particle analysis has been reported. The proposed approach contains two stages. In the first stage, the sparse 3D point-cloud model was built by multi-view image contour fitting. During this stage, the rotation axis of the moving particle and the rotation angle between two adjacent images were determined. In the second stage, the dense 3D point-cloud model was generated using the NCS-based interpolation. The developed 3D particle reconstruction method was evaluated by comparing to LSCM images. The results showed that the constructed dense 3D models have high accuracy in height and kurtosis (Sa, Sq and Sku) as compared with the information obtained by the LSCM examinations. Moreover, the developed 3D reconstruction method can provide multi-view features of the wear particles, which is valuable for the development of wear analysis in machine condition monitoring.

Future work is prepared for developing the dense point-cloud interpolation algorithm to reduce 3D

reconstruction errors. The CMOS camera will be developed to increase the image resolution to monitor small particles less than 20 μm. Moreover, the particle surface features will be extracted from high resolution images to construct 3D particle surface by referencing stereo matching of binocular images.

CRediT authorship contribution statement

Yeping Peng: Conceptualization, Methodology, Writing - original draft, Writing - review & editing. Zhengbin Wu: Writing - original draft, Methodology. Guangzhong Cao: Supervision. Song Wang: Resources. Hongkun Wu: Writing - review & editing. Chaozong Liu: Writing - Review & editing. Zhongxiao Peng: Writing - review & editing.

Declaration of competing interest

The authors declare that they have no known competing financial interests or personal relationships that could have appeared to influence the work reported in this paper.

Acknowledgement

This work is supported by the National Natural Science Foundation of China (Grant Nos. 51905351 and U1813212), Natural Science Foundation of Guangdong Province, China (Grant No. 2018A030310522), and the Science and Technology Planning Project of Shenzhen Municipality, China (Grant Nos. JCYJ20190808113413430 and JCYJ20190807144001746). Chaozong Liu would like to acknowledge the support from Royal Society via an International Exchange program (Grant No: IEC\NSFC\191253).

References

[1] H.K. Wu, R.W. Li, N.M. Kwok, Y.P. Peng, T.H. Wu, Restoration of low-informative image for robust debris shape measurement in on-line wear debris monitoring, Mech. Syst. Signal Process. 114 (2019) 539-555.

[2] A. Kumar, S.K.Ghosh, Size distribution analysis of wear debris generated in HEMM engine oil for reliability assessment: A statistical approach, Measurement 131 (2019) 412-418.

[3] S. Sardar, S.K. Karmakar, D. Das, High stress abrasive wear characteristics of Al 7075 alloy and 7075/ Al_2O_3 composite, Measurement 127 (2018) 42-62.

[4] Y.P. Peng, J.H. Cai, T.H. Wu, A hybrid convolutional neural network for intelligent wear particle classification, Tribol. Int. 138 (2019) 166-173.

[5] W. Cao, H. Zhang, N. Wang, H.W. Wang, Z. Peng, The gearbox wears state monitoring and evaluation based on on-line wear debris features, Wear 426 (2019) 1719-1728.

[6] J. Song, F.F. Chen, Y.H. Liu, S. Wang, X. He, Z.H. Liao, X.H. Mu, M.Y. Yang, W.Q. Liu, Z. Peng, Insight into the wear particles of PEEK and CFRPEEK against UHMWPE for artificial cervical disc application: Morphology and immunoreaction, Tribol. Int. 144 (2020) 106093.

[7] H.W. Fan, S.Q. Gao, X.H. Zhang, X.G. Cao, Intelligent recognition of ferrographic images combining optimal CNN with transfer learning introducing virtual images, IEEE Access 8 (2020) 137074-137093.

[8] X. Qiu, N.U.H. Tariq, J.Q. Wang, J.R. Tang, L. Gyansah. Microstructure, microhardness and tribological behavior of Al_2O_3 reinforced A380 aluminum alloy composite coatings prepared by cold spray technique. Surf. Coat. Technol. 350 (2018) 391-400.

[9] M. Merola, A. Ruggiero, J.S.D. Mattia, On the tribological behavior of retrieved hip femoral heads affected by metallic debris. A comparative investigation by stylus and optical profilometer for a new

roughness measurement protocol, Measurement 90 (2016) 365-371.

[10] S. Wang, T.H. Wu, L.F. Yang, N.M. Kwok, T. Sarkodie-Gyan, Three-dimensional reconstruction of wear particle surface based on photometric stereo, Measurement 133 (2019) 356-360.

[11] T.H. Wu, Y.P. Peng, S. Wang, F. Chen, N.M. Kwok, Morphological feature extraction based on multiview images for wear debris analysis in on-line fluid monitoring, Tribol. Trans. 60 (2017) 408-418.

[12] M. Hakim, A. Ghazdali, A. Laghrib, A multi-frame super-resolution based on new variational data fidelity term, Appl. Math. Model. 87 (2020) 446-467.

[13] J.J. Liu, A. Ni, G.X. Ni, A nonconvex $L_1(L_1\text{-}L_2)$ model for image restoration with impulse noise, J. Comput. Appl. Math. 378 (2020) 112934.

[14] S.J. Liu, Q.M. Liao, J.H. Xue, F. Zhou, Defocus map estimation from a single image using improved likelihood feature and edge-based basis, Pattern Recognit. 107 (2020) 107485.

[15] Y.P. Peng, T.H. Wu, S. Wang, Y. Du, N. Kwok, Z. Peng, A microfluidic device for three-dimensional wear debris imaging in online condition monitoring, Proc. Inst. Mech. Eng. Part J J. Eng. Tribol. 231 (2017) 965-974.

[16] H.K. Wu, N.M. Kwok, S.L. Liu, T.H. Wu, Z.X. Peng, A prototype of on-line extraction and three-dimensional characterisation of wear particle features from video sequence, Wear 368 (2016) 314-325.

[17] Y.P. Peng, J.H. Cai, T.H. Wu, G.Z. Cao, N.M. Kwok, S.X. Zhou, Z.X. Peng, Online wear characterisation of rolling element bearing using wear particle morphological features, Wear 430 (2019) 369-375.

[18] X.P. Yan, X.J. Xu, C.X. Sheng, C.Q. Yuan, Z.X. Li, Intelligent wear mode identification system for

marine diesel engines based on multi-level belief rule base methodology, Meas. Sci. Technol. 29 (2018) 1361-6501.

[19] S. Wang, T.H. Wu, K.P. Wang, Z. Peng, N.M. Kwok, T. Sarkodie-Gyan, 3-D particle surface reconstruction from multiview 2-D images with structure from motion and shape from shading, IEEE T. Ind. Electron. 68 (2021) 1626-1635.

[20] Y.P. Peng, T.H. Wu, S. Wang, Z.X. Peng, Wear state identification using dynamic features of wear debris for on-line purpose, Wear 376 (2017) 1885-1891.

[21] Y.P. Peng, T.H. Wu, S. Wang, Z.X. Peng, Oxidation wear monitoring based on the color extraction of on-line wear debris, Wear 332 (2015) 1151-1157.

[22] X.K. Lu, Y.Y. Zhao, D.J.C. Dennis, Fluid flow characterisation in randomly packed microscale porous beds with different sphere sizes using micro-particle image velocimetry, Exp. Therm. Fluid Sci. 118 (2020) 110136.

[23] J.F. Richardson, J.H. Harker, J.R. Backhurst, Chemical Engineering: Particle Technology and Separation Processes, fifth ed., Butterworth Heinemann, United Kingdom, 2013.

[24] H. Long, L.W. Sang, Z.J. Wu, W. Gu, Image-based abnormal data detection and cleaning algorithm via wind power curve, IEEE Trans. Sustain. Energy 11 (2020) 938-946.

[25] V. Drakopoulos, P. Manousopoulos, On non-tensor product bivariate fractal interpolation surfaces on rectangular grids, Math. 8 (2020) 525.

[26] G. Hesamian, M.G. Akbari, Fuzzy spline univariate regression with exact predictors and fuzzy responses, J. Comput. Appl. Math. 375 (2020) 112803.

[27] F.D. Accio, F.D. Tommaso, O. Nouisser, N. Siar, Rational Hermite interpolation on six-tuples and scattered data, Appl. Math. Comput. 386 (2020) 125452.

[28] C.P. Lin, J. Cabrera, D.Y.W. Yu, F. Yang, K.L. Tsui, SOH estimation and SOC recalibration of lithium-Ion battery with incremental capacity analysis & cubic smoothing spline, J. Electrochem. Soc. 167 (2020) 090537.

[29] K.M. Marcoulides, J. Khojasteh, Analyzing longitudinal data using natural cubic smoothing splines, Struct. Equ. Model. 25 (2018) 965-971.

[30] International Organization for Standardization, Geometrical product specifications (GPS) - Surface texture: Areal Part 2: Terms, definitions and surface texture parameters, Int. Stand. ISO. (2012).